



Full Length Article

Rough Fe₃O₄/gold nanostructure enhanced fluorescence of quantum dots for *Salmonella typhimurium* detection in cabbageAbdulhakeem Alzahrani^a, Tawfiq Alsulami^{a,*}, Ahmad Mohammad Salamatullah^a, Hind Saeed Alzahrani^b^a Department of Food Science & Nutrition, College of Food and Agricultural Sciences, King Saud University, Riyadh 11451, Saudi Arabia^b Department of Physics, College of Science, Taif University, Taif 21944, Saudi Arabia

ARTICLE INFO

Keywords:

Urchin-like Fe₃O₄@Au NPs
Gold quantum dots
Fluorescence enhancement
Salmonella typhimurium detection

ABSTRACT

Salmonella typhimurium (*S. typhimurium*) is a leading biological factor of foodborne diseases. A sensitive detection for *S. typhimurium* is crucial to controlling fresh vegetable-related outbreaks. Here, fluorescence-based *S. typhimurium* detection in fresh cabbage samples has been reported which capitalizes on the plasmon-exciton interaction between non-spherical gold nanoparticles-covered iron oxide nanoparticles (Fe₃O₄@Au NPs) and gold quantum dots (Au QDs). Firstly, new synthesis methods for non-spherical Fe₃O₄@Au NPs and Au QDs are reported. Then, a two-fold emission enhancement and shortening of the lifetime were achieved from urchin-like NPs compared with those of spherical NPs. This finding was utilized for the detection of *S. typhimurium*. Results revealed that the changes in fluorescence emission were linearly correlated with the concentration of *S. typhimurium* within the range of 100–1000 colony forming unit per milliliter (CFU mL⁻¹) and the limit of detection was 32 CFU mL⁻¹ in fresh cabbage.

1. Introduction

Cabbage is a popular leafy vegetable all around the world and can be consumed in many ways. The simplest way to consume it is to include it raw in salads. However, raw cabbage can be contaminated with pathogenic bacteria along different steps of the farm-to-fork continuum, which can result in a potentially fatal outcome. One of the most common pathogenic bacteria associated with leafy vegetable outbreaks is *Salmonella*, a gram-negative bacterium (Habib et al., 2023). *Salmonella* is reported to cause 180 million cases of foodborne illness with roughly 298,496 cases of deaths worldwide (Ehuwa et al., 2021). In Saudi Arabia, *Salmonella* represents one of the most frequent agents associated with foodborne illness. Particularly, *Salmonella typhimurium* (*S. typhimurium*) is one of the significant strains of *Salmonella* spp, that can be colonized in many foods, with consumption of uncooked vegetables being the most common way to ingest *S. typhimurium*. Hence, the detection of pathogenic bacteria in food is a key step in preventing foodborne illnesses. Enzyme-linked immunosorbent assay (ELISA) and polymerase chain reaction (PCR) are common detection methods of *S. typhimurium*. Those methods are highly accurate, but have several drawbacks such as longer detection time, and complexity in operation

limiting their use for on-site applications (Wang et al., 2020). Therefore, a rapid and accurate quantification of *S. typhimurium* in the field has become an important target to reduce the risk associated with food consumption. The advancement of nanotechnology in biosensing areas provide an opportunity to develop a rapid and sensitive detection system (Ahmed et al., 2024; Ahmed et al., 2020; Ahmed et al., 2021; Ahmed et al., 2022). Generally, fluorescence techniques provide a much faster and more sensitive detection alternative compared to the other techniques (Viter et al., 2018; Myndrul et al., 2017). The enhancement of fluorescence emission at the close proximity of plasmonic surface has received a lot of interest that enables to develop highly sensitive biosensor. Here, the excitation wavelength of fluorophore couple with the plasmon resonance energy and create a stronger excited regime. While electrons dropped from the excited to ground state, a stronger emission from the fluorophore occurs that may enable the development of an ultra-sensitive biosensor. In this case, the shape of metallic nanoparticles has a significant role in varying the fluorescence emission wavelength (Alzahrani et al., 2023). For example, plasmonic scattering on rough surface can confine more energy in the regime that ultimately boosting the fluorescence enhancement while come to closer of the fluorophore through biological or chemical interaction.

* Corresponding author.

E-mail address: talsulami@ksu.edu.sa (T. Alsulami).

Hence, a lot of research articles have focused on preparing different geometries of NPs over the last several years. The size and shape have a strong impact on the properties of nanoparticles. In particular, a lot of researchers have paid attention to the fabrication of non-spherical-shaped NPs (Ahmed et al., 2014; Ahmed et al., 2017; Ahmed et al., 2017; Ahmed et al., 2018). The fabrication of non-spherical NPs is driven by subtle kinetic differences in the growth of the precursor nanocrystals generated in the reaction process. Typically, the prepared non-spherical-shaped NPs are thermodynamically unstable and tend to transform into spherical ones with time. Therefore, the preparation methods are usually scrupulously modified to control the epitaxial growth mechanism so that anisotropic NPs are formed.

Moreover, non-spherical core-shell structured nanoparticles have received huge research focus because of their outstanding characteristics, for example, the inner core and an outer shell of the nanoparticles can be made of different materials that generate different multiple properties in a single structure, expanding their application to diverse areas. The properties of non-spherical core-shell structured nanoparticles can be tuned by varying the shell thickness, and shell materials in addition to their size and shape. Importantly, the core-shell structure can protect the materials from aggregation, improve photo-stability and biocompatibility (Cheng et al., 2020; Eremin et al., 2019; Li et al., 2023; Wu et al., 2023). Chiefly, the fascinating bifunctional (magnetic and optical) properties of gold (Au)-covered magnetic nanoparticles (MNP@Au NPs) allow for their application in many different areas, for example, diagnosis, imaging, and drug delivery (Félix et al., 2019; Gessner et al., 2022; Baniukevic et al., 2013). Though a fluorescence enhancement-based *S. typhimurium* detection method using MNPs, spherical Au NPs and quantum dots (QDs) has been reported recently, the preparation of non-spherical magneto-plasmonic core-shell structure and their uses for fluorescence enhancement-based *S. typhimurium* detection has still not been reported which might offer a much simpler detection technique (Wang et al., 2020).

Herein, we present a synthesis route to a uniquely shaped metallic nano-complex, i.e., urchin-shaped Au-coated iron oxide nanoparticles (Fe_3O_4 @Au NPs) with tunable diameters of roughly 105–185 nm and strong magnetization. Both Au NPs and Fe_3O_4 NPs are well-known for their environment-friendly nature. Here, the synthesis method uses sodium citrate and triethanolamine through a seed-mediated growth approach. Then, the unique variations in the plasmon-induced fluorescence intensity caused by the varying surface topographies of spherical and urchin-like NPs were observed in order to characterize the optical and electromagnetic properties of the NPs. We also proposed a possible mechanism for the luminescence enhancement caused by the surface morphology. Furthermore, the enhanced fluorescence of QDs on plasmonic rough-surface was utilized to develop a fluorescence-based *S. typhimurium* detection (Scheme S1).

2. Experimental details

2.1. Materials

Tetrachloroauric(III) acid trihydrate ($\text{HAuCl}_4 \cdot 3\text{H}_2\text{O}$, 99.9 %), sodium malate, trisodium citrate ($\text{Na}_3\text{C}_6\text{H}_5\text{O}_7$), triethanolamine, $\text{FeCl}_3 \cdot 6\text{H}_2\text{O}$, $\text{FeCl}_2 \cdot 4\text{H}_2\text{O}$, ammonia solution (25 %), *Staphylococcus aureus*, *Escherichia coli*, *shawnelle oneidensis*, *enterobacter aerogenes*, *proteus mirabilis*, *citrobacter freundii*, *citrobacter diversus*, *enterobacter cloacae* and *bacillus*, triethanolamine (98 %) were received from Sigma-Aldrich (Oakville, Canada). *S. typhimurium* aptamers (5'-NH₂-AGT AAT GCC CGG TAG TTA TTC AAA GAT GAG TAG GAA A AGA-3') were purchased from Creative Biolabs (NY, USA).

2.2. Synthesis of Fe_3O_4 @citrate NPs

The citrate-capped Fe_3O_4 NPs were prepared through a coprecipitation technique (Aghari et al., 2023). Shortly, $\text{FeCl}_3 \cdot 6\text{H}_2\text{O}$ (1.622 g)

and $\text{FeCl}_2 \cdot 4\text{H}_2\text{O}$ (0.994 g) were mixed in a beaker of water (40 mL) and stirred gently for 5 min. Then, the ammonia solution (5 mL) was mixed with the reaction mixture, which was then left alone for 15 min. Afterward, 4.4 g of sodium citrate was mixed with the above reaction solution and the temperature was set up to 90 °C for 30 min. After cooling down the reaction solution to room temperature, the black-colored precipitate was obtained. The sample was centrifuged (6500 rpm, 20 min) and washed several times with water and dried under vacuum conditions.

2.3. Preparation of Fe_3O_4 @Au composite NPs

At first, HAuCl_4 solution (20 mL, 0.5 mmol/L) was heated to boiling temperature alongside vigorous stirring. Then, different volumes of Fe_3O_4 @citrate NPs were added, spontaneously changing the solution color from brown to burgundy. The Fe_3O_4 @Au NPs precipitates were separated through centrifugation (6500 rpm, 20 min) and redispersed in water for the following experiments.

2.4. Preparation of urchin-like Fe_3O_4 @Au NPs

Urchin-like Fe_3O_4 @Au NPs were prepared based on a reported article with some modifications (Han et al., 2023). To do so, various volumes of Fe_3O_4 @Au seeds (100–500 μL), 22 μL of 1 % sodium citrate (1 %, 22 μL), and triethanolamine (1000 μL , 30 mmolL^{-1}) were added into the aqueous solution of HAuCl_4 (10 mL, 0.25 mmol/L) and strongly stirred at room temperature. The change in color (bluish) will indicate the successful synthesis of urchin-like Fe_3O_4 @Au NPs. The Fe_3O_4 @Au NPs precipitates were separated through centrifugation (6500 rpm, 20 min) and redispersed in water for the following experiments.

2.5. Preparation of Au QDs

To prepare Au QDs, Au NPs were first synthesized using sodium malate. Briefly, 1 mL of sodium malate solution (1 mmol/L) was added to 20 mM of HAuCl_4 (20 mL) solution and heated at 100 °C for 30 min. The initial light-yellow color of the solution turned reddish indicating the formation of Au NPs. After centrifuging three times (5000 rpm, 30 min), the purified Au NPs were dispersed in MilliQ water. Then, 10 mL of Au NPs solution was autoclaved at 200 °C for 2 h. At this stage, the initial reddish color of the solution turned to deep yellow indicating the formation of Au QDs. At first, the synthesized Au QDs was purified through centrifugation (15000 rpm, 30), then again purified by dialysis. The fluorescence emission of the purified Au QDs was measured using fluorescence spectroscopy and the sample was stored at 4 °C before further uses.

2.6. Preparation of nanocomposite film for plasmon enhancement

At first, glass slides (2 × 10 cm) were cleaned using piranha solution for 1 h and washed with deionized water. Then, 1 wt% aqueous solution of positively charged poly(dimethyldiallylammonium chloride) (PDDA) and a 1 mg/mL aqueous solution of negatively charged poly(acrylic acid) (PAA) were prepared separately. The glass slides were first immersed into the PDDA solution for 10 min. Then, the slides were washed with water to remove any unbound polymers and dried with N₂ gas. Next, the slides were immersed in the PAA solution for 10 min and then washed and dried as before. This method was performed to build the (PDDA/PAA)₂/PDDA base layers. These slides were then immersed in spherical-shaped Fe_3O_4 @Au NPs solution for 10 min and, subsequently, in the urchin-like Fe_3O_4 @Au NPs solution for 10 min. After washing and drying, the slides were immersed into a PDDA/PAA/PDDA solution to make a spacer layer between the metallic NPs surface and QDs. Lastly, the slides were immersed in Au QDs (2 mmol/L) solution for 10 min.

2.7. Conjugation of aptamer with nanocomposite film

The rough film of $\text{Fe}_3\text{O}_4@\text{Au}$ nanostructure prepared above was mixed with an EDC (10 mM) and NHS (4 mmol/L) solution to activate the carboxyl group of the film. Then, the aptamer (10 mmol/L) was added to the film and kept at 37°C for 1 h. The aptamer-modified film was then washed three times with PBS buffer to remove loosely bound or unbound aptamers and kept at 4°C before further experiments.

2.8. Conjugation of aptamer with Au QDs

2 mL of Au QDs solution was added to the EDC (10 mmol/L) and NHS (4 mmol/L) solution and kept under dark conditions for 30 min. Then, the aptamer (10 mmol/L) was added to the Au QDs solution and kept at 37°C for 1 h.

2.9. Detection of *S. Typhimurium* using aptamer modified nano-complex

In this study, aptamer-modified $\text{Fe}_3\text{O}_4@\text{Au}$ and Au QDs form a nano-complex in the presence of *S. typhimurium* and help to quantify *S. typhimurium* concentration. Shortly, aptamer-conjugated $\text{Fe}_3\text{O}_4@\text{Au}$ (100 μL) containing various concentrations of *S. typhimurium* in PBS buffer were added in the different wells of 96-well plates. Then, aptamer-conjugated Au QDs (100 μL) were added to each well, and the fluorescence response within different wells was measured using fluorescence spectroscopy. For the real-life application of the proposed detection method, a fresh cabbage was purchased from the local market and soaked in PBS buffer (10 g) for 1 h. Then, the cabbage was crushed using a blender and filtered to remove impurities. The differently concentrated solution was prepared by mixing *S. typhimurium*, aptamer conjugated $\text{Fe}_3\text{O}_4@\text{Au}$ (100 μL) & Au QDs, and the changes in fluorescence emission of the mixtures were monitored using fluorescence spectroscopy.

2.10. Characterization

The absorbance and fluorescence properties of NPs were monitored using BioTek spectrophotometer (Synergy H1, USA). The shape and sizes of the NPs were examined by high-resolution transmission electron microscope (HR-TEM) (80–300 LB, Hillsboro, USA) and atomic force microscope (Veeco, diInnova). Zetasizer (Malvern Instruments, Nano ZS) was used for surface charge measurement. The particles were characterized by an X-ray powder diffractometer (XRD; D8 FOCUS 2.2 kW, Bruker, Germany). The lifetime decay profile of QDs was checked using Horiba Lifetime Fluorometer (DeltaFlex TCSPC, London, ON, Canada).

The statistical differences among the datas were computed using one way analysis of variance (ANOVA) and the post hoc Tukey test at the $p < 0.05$ significance level. The graphs were created using OriginPro-2020.

3. Results and discussion

3.1. Spectroscopic and microscopic characterization of nanomaterials

The optical and electromagnetic properties of Au NPs are prone to changes depending on their sizes and shapes. Particularly in our experiments, a non-spherical shape with many epitaxial growths was intentionally synthesized, inducing irregular optical properties. Fig. 1 presents the experimental data for two different types of core-shell $\text{Fe}_3\text{O}_4@\text{Au}$ NPs, i.e., spherical and urchin-like NPs. First, an Au shell was formed around the Fe_3O_4 core NPs, which is the common procedure for producing many different types of NPs. The Fe_3O_4 NPs were directly added to a boiling HAuCl_4 solution, where the Au salts in the solution resided. Sodium citrates on the Fe_3O_4 NPs' surfaces reduced the gold salts in the solution to form an Au shell (this is the final step of spherical NP synthesis). After that, the urchin-like $\text{Fe}_3\text{O}_4@\text{Au}$ core-shell NPs were

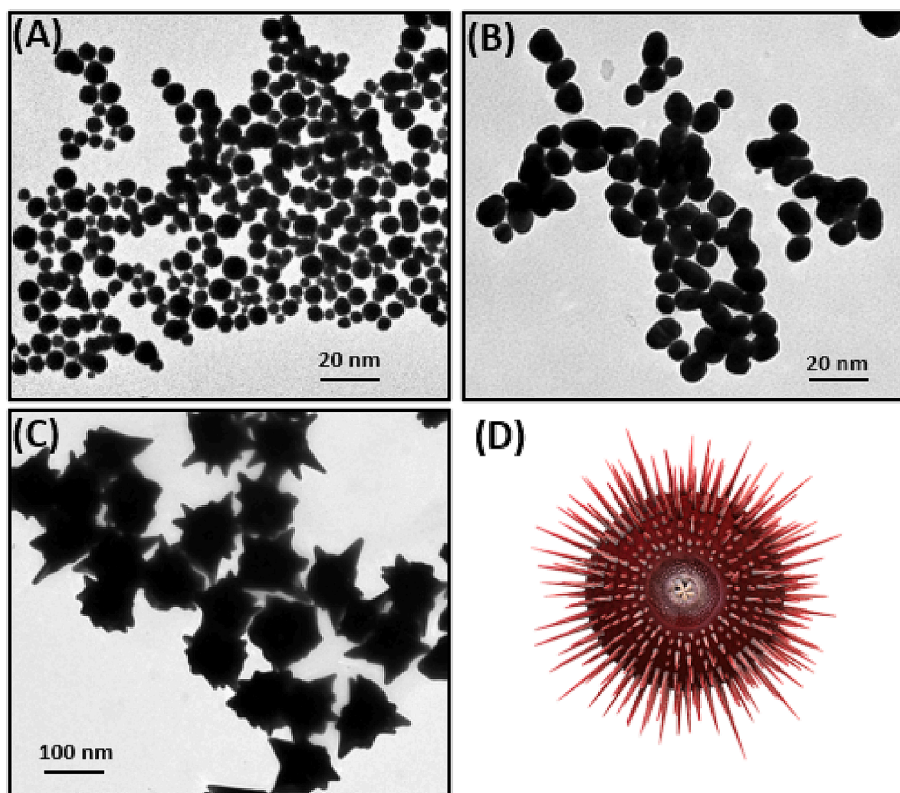


Fig. 1. TEM images of (A) Fe_3O_4 NPs, (B) $\text{Fe}_3\text{O}_4@\text{Au}$ NPs, and (C) urchin-like $\text{Fe}_3\text{O}_4@\text{Au}$ NPs and (D) a 3D schematic presentation of an urchin-like $\text{Fe}_3\text{O}_4@\text{Au}$ NP.

synthesized in the presence of citrate and triethanolamine through a seed-mediated growth approach. Fig. 1 displays representative TEM images of the Fe_3O_4 NPs (Fig. 1A), spherical Fe_3O_4 @Au NPs (Fig. 1B), and urchin-like Fe_3O_4 @Au NPs (Fig. 1C). It can be clearly observed in the TEM micrograph that the Fe_3O_4 NPs are almost spherical in shape and have a size of ~ 10 nm and the solution color is yellow. We added the Fe_3O_4 @citrate solution to the HAuCl_4 solution to reach a total volume of 10 mL, which led to the synthesis of Fe_3O_4 @Au NPs (Fig. 1B). At this point, the solution color changed to purple. After adding triethanolamine (1000 μL) and Fe_3O_4 @Au seeds (1000 μL) into the reaction system, urchin-like Fe_3O_4 @Au NPs with many spikes were obtained (Fig. 1C). The branches were carefully counted in the TEM images. The average number of branches per NP was approximately 25–30. The sizes of the urchin-like Fe_3O_4 @Au NPs were about 185 nm, and the solution color was blue. The diameters of urchin-like NPs were tunable from 105 to 185 nm by altering the feed ratio of the seeds and triethanolamine. A detailed X-ray study was carried out to characterize the composition of significant features, i.e., core and branch of urchin NP (Fig. S1 and Table S1).

In this study, Fe_3O_4 @Au seeds with diameters of about 30 nm were used for the synthesis of urchin-like Fe_3O_4 @Au NPs. Here, trisodium citrate acted as a surface ligand and both citrate and triethanolamine acted as reductants during the synthesis of the urchin-like Fe_3O_4 @Au NPs. A step-by-step reduction process, i.e., $\text{Au}^{\text{III}} \rightarrow \text{Au}^{\text{I}} \rightarrow \text{Au}^0$ was followed during the synthesis reaction. However, the weak reduction ability of trisodium citrate at room temperature allows only the conversion of Au^{III} to Au^{I} instead of Au^0 . However, the high selectivity of triethanolamine to reduce Au^{I} to Au^0 on the Fe_3O_4 @Au seed surface in the presence of gold seeds permits the completion of the stepwise reduction process (Han et al., 2023). Moreover, triethanolamine controlled the formation of an urchin-like structure on the surface of

Fe_3O_4 @Au NPs. To test this, we examined the ultraviolet–visible (UV–visible) spectra of the solution for triethanolamine-assisted reduction of HAuCl_4 in the presence and absence of particle seeds. We examined the kinetics of the reaction solution; no particle formation was observed until the seeds were added (Fig. S2). This demonstrates the selectivity of triethanolamine and the importance of the seeds.

The analysis of HR-TEM and powder XRD data confirmed the existence of highly active facets on the urchin-like Fe_3O_4 @Au NPs (Fig. 2). Fig. 2D illustrates the XRD pattern of urchin-like Fe_3O_4 @Au NPs. The XRD peaks of urchin-like Fe_3O_4 @Au NPs matched perfectly with both its precursor materials: Au and Fe_3O_4 bulk counterparts. The diffraction peaks of urchin-like Fe_3O_4 @Au NPs observed at the (111), (200), (220), (311), and (222) positions can be assigned to Au planes structure. The diffraction peaks obtained at (220), (311), and (440) positions can be assigned to the Fe_3O_4 plane structure (Adhikari et al., 2022). The finding of XRD peaks revealed the polycrystalline nature of urchin-like Fe_3O_4 @Au NPs. In addition, the strongest diffraction peak found at the (111) position reveals the formation of a branched structure of the Fe_3O_4 @Au NPs could be attributed to the rapid buildup of Au^0 on the (111) lattice planes. The HR-TEM observation of the branches confirmed this hypothesis (Fig. 2B). For example, the interplanar distances of 0.211 and 0.196 nm were observed and found to be consistent with the (111) and (200) planes of Au crystals. These findings revealed that the direction of the Fe_3O_4 @Au NPs structure formation was vertical towards the (111) plane and that the plane has a high-energy facet.

Au NPs have strong absorption peaks in the visible region because of their surface plasmon properties. Pointedly, citrate-capped Au NPs in water exhibit a strong absorbance peak at around 520 nm. The absorbance spectra of the Fe_3O_4 @Au NPs prepared with Fe_3O_4 NP solution were presented in the Fig. S3A. There were no noticeable absorption peaks of Fe in the visible regions of the spectra of the pure Fe_3O_4 NP

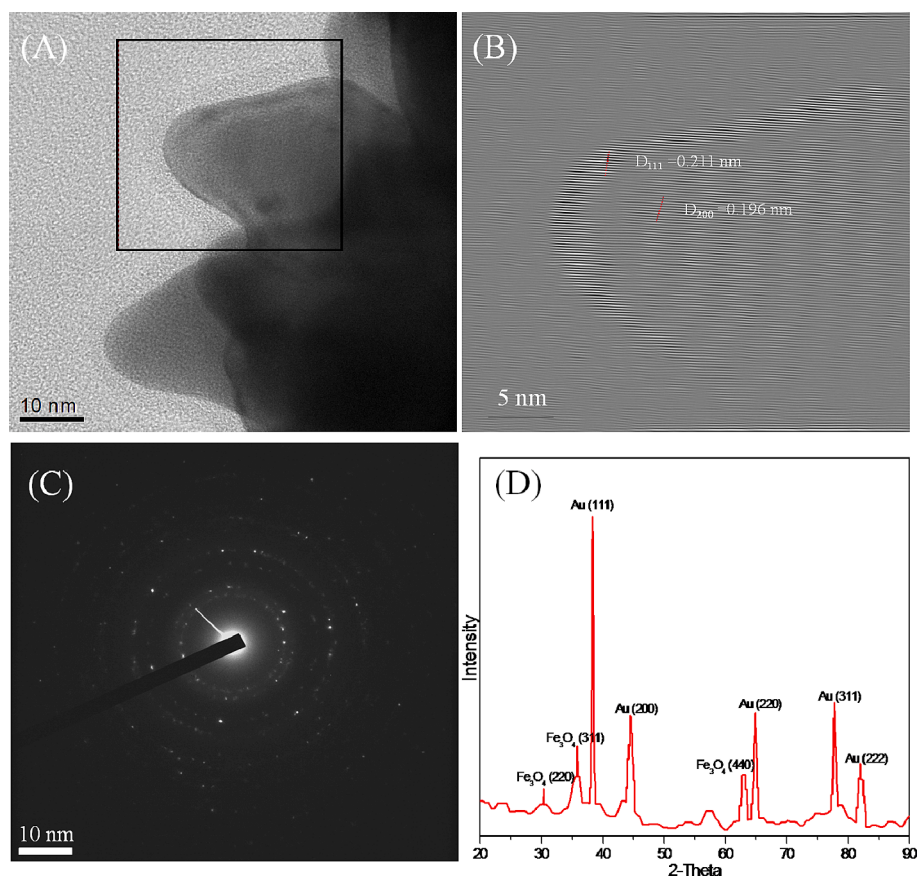


Fig. 2. (A) HR-TEM image of one branch of the urchin-like NPs. (B) Growth direction of the branch. (C) Selected area electron diffraction (SAED) pattern of the urchin-like NPs. (D) XRD pattern of urchin-like NPs.

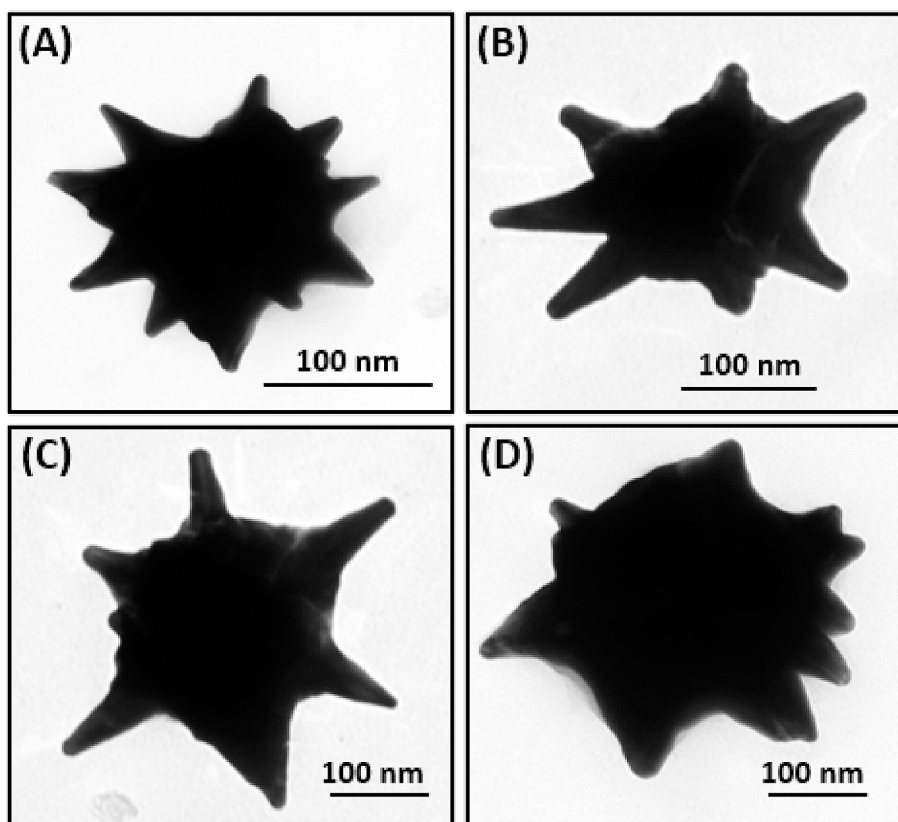


Fig. 3. TEM images of urchin-like $\text{Fe}_3\text{O}_4@Au$ NPs for different seed amounts: (A) 100 μL , (B) 200 μL , (C) 300 μL , and (D) 400 μL .

solution, however, absorbance peaks in the range of 470–800 nm were observed for the $\text{Fe}_3\text{O}_4@Au$ NP solutions, revealing the development of an Au shell on the top of Fe_3O_4 NPs.

The peak wavelength changed from 600 to 670 nm in the UV–visible absorption spectra by increasing the reactive volume from 100 to 500 μL (Fig. S3B), indicating that the diameters of the urchin-like NPs can be

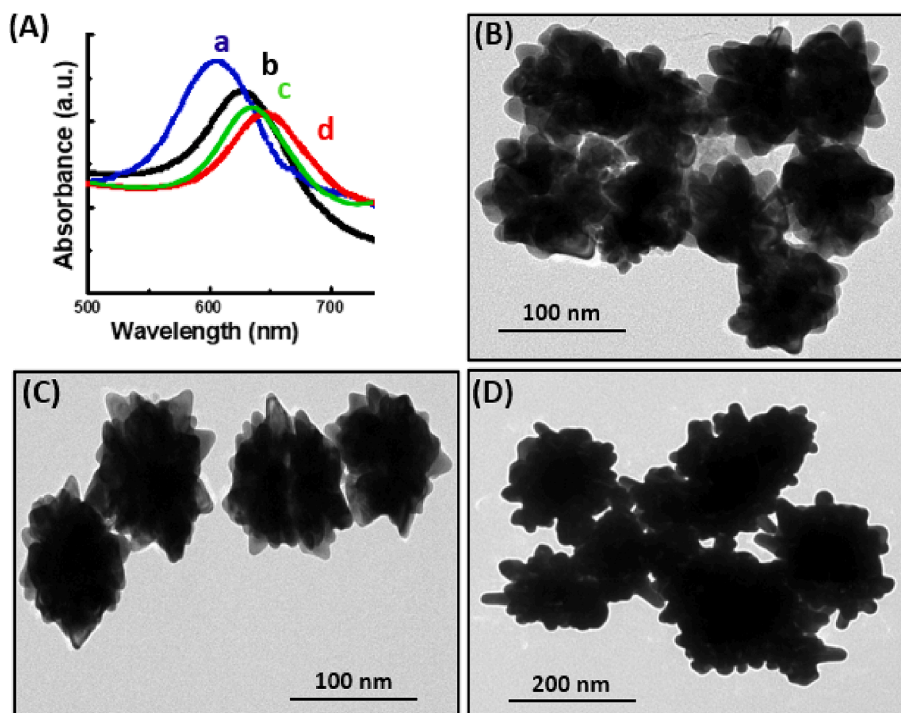


Fig. 4. (A) UV–visible absorption spectra of urchin-like $\text{Fe}_3\text{O}_4@Au$ NPs in different volumes of triethanolamine: 125 μL (a), 250 μL (b), 500 μL (c), and 1000 μL (d). The amounts of seeds and sodium citrate were fixed at 100 and 22 μL , respectively. (B–D) TEM images of urchin-like $\text{Fe}_3\text{O}_4@Au$ NPs in different volumes of triethanolamine: (B) 125 μL , (C) 500 μL , and (D) 1000 μL .

controlled in the range from 175 nm to 95 nm (Fig. 3). Here, the higher Au⁰/seed ratio of the seed solution helps to increase the growth of the NPs. It is preferable to control the size of the Au nanocrystals by varying the initial concentration of citrate to that of Au solution. In our reaction, the spherical Fe₃O₄@Au NPs were used as the nucleation centers of Au for forming urchin-like Fe₃O₄@Au core-shell NPs. Hence, a faster reduction was observed with increasing the reaction ratio of Fe₃O₄@Au/HAuCl₄. This depleted the solution of precursor atoms available for growth, leading to smaller particles. This mechanism matched well with the results of TEM images, as shown in Fig. 3 (A-D). Furthermore, branched growth was facilitated rather than isotropic growth because of the higher Au⁰/seed ratio, and the type of growth also depended on the amount of triethanolamine.

The triethanolamine concentration-dependant properties of the Fe₃O₄@Au NPs were presented in Fig. 4. The absorption peak of the Fe₃O₄@Au NPs moved from 610 to 650 nm with increasing amount of triethanolamine from 125 to 1000 μL (Fig. 4A). The particle size and number of branches increased (Fig. 4B, 4C, and 4D) as well which indicated that the addition Au⁰ in the reaction system has played a significant role in the construction of urchin-like Fe₃O₄@Au NPs. The increase in the amount of triethanolamine accelerates the conversion of Au¹ to Au⁰, forming the urchin-like structure of NPs. Although the absorption peak of the NPs formed with the addition of 1000 μL of triethanolamine generally appears at longer wavelengths than that of NPs formed with 500 μL, the opposite result was occasionally observed (Fig. 4A). This meant that 1000 μL of triethanolamine was adequate for the present reduction process. Most probably, the extra triethanolamine had adsorbed on the surface of the NPs and suppressed its growth. This result implies that there are multiple functions of triethanolamine, which acts both as a reducing and capping agent.

3.2. Modifications of fluorescence emission of QDs on rough surface

The coupling of excitonic properties of QDs and plasmonic properties of metallic nanoparticles at a nanoscale distance widens its applications in diverse areas. In this paper, we demonstrated the photoluminescence (PL) changes of QDs attached to metallic films with different controlled surface roughness. The surface roughness of a metallic film can have a unique effect on achieving a strong coupling regime due to the scattering of plasmonic energy. Layer-by-layer (LBL) assembly was used as a bottom-up nanofabrication technique to make nanocomposite films. A schematic illustration of metal-enhanced fluorescence is shown in Scheme S1.

In our experiment, we deposited equal amounts of spherical and urchin-like Au NPs on a glass substrate, which was confirmed by measuring the optical density (OD) of the surface. The OD of each film was fixed at 0.6. The root-mean-square (rms) roughness R_{rms} was observed using topographic images obtained from AFM measurements in the tapping mode, as shown in Fig. S4A and S4B. The R_{rms} of the spherical gold NP surface is about 1.2772 ± 0.21 nm, whereas, for urchin-like gold NPs, the R_{rms} is 2.2286 ± 0.19 nm. A comparison of the R_{rms} values of the two surfaces indicates that urchin-like NPs produced more defects in the film because of the uneven surface structure in the nanoscale process. It is known that rough films are more advantageous in enhancing optical properties (Ahmed et al., 2014). PL spectra of the samples were recorded using a 380 nm excitation xenon lamp. Fig. S4C shows the PL spectra taken for Au QDs on two different gold surfaces. We found more than twofold emission enhancement of the Au QDs deposited on urchin-like gold compared to that of the spherical gold surface. PL decay was studied with a 380 nm laser excitation source at room temperature. The curves in Fig. S4D show the PL time profiles of the QDs on two different gold surfaces. The decay time of Au nanocrystals on urchin-like gold surfaces (3.23 ± 0.06 ns) is shorter than that for spherical gold surfaces (4.10 ± 0.10 ns). It is well known that the photoluminescence of a semiconductor nanoparticle is significantly enhanced when the local surface plasmon field of metal is nearby. It is

also noticeable that the local field effect can be achieved by using rough metal surface instead of metal nanoparticles. Usually, the light field is diffraction-limited in a nano-size dielectric slit. However, the field is dramatically strengthened in the case of metallic slit as the surface plasmon field is concentrated at a local spot. Therefore, a similar effect can be expected in an urchin-like Fe₃O₄@Au structure as the local field near the urchin tips is possibly stronger than the dipole field of a spherical metal nanoparticle. In fact, we observed over twofold enhancement of the photoluminescence in urchin-like - Fe₃O₄@Au structures in comparison to spherical Au nanoparticles. The decay time of Au QDs is shortened whereas in the absence of metal structures, there are no changes to the decay time. Regarding the sharp tip of an urchin-like structure, one may be concerned with non-radiative energy transfer or quenching near the short inter-molecular distance. However, the decay time constant barely changes in the case of spherical Au nanoparticles despite the photoluminescence enhancement. These results suggest that the enhancement by the urchin-like Fe₃O₄@Au is possibly associated with the surface plasmonic local field effect in the nanotips of the urchin-like Fe₃O₄@Au structure.

3.3. Detection of *S. typhimurium*

The enhancement of fluorescence emission on urchin-like - Fe₃O₄@Au NPs film was utilized for the detection of sensitive *S. typhimurium*. The conjugation of the target specific aptamer with urchin-like Fe₃O₄@Au NPs film and Au NPs was confirmed through the ELISA method. As shown in Figure S5, a higher absorbance value was achieved for aptamer-conjugated urchin-like Fe₃O₄@Au NPs film and Au NPs indicating the successful conjugation of aptamer with urchin-like Fe₃O₄@Au NPs film and Au NPs.

Then, different concentrations of *S. typhimurium* solutions were added to the aptamer with urchin-like Fe₃O₄@Au NPs film and Au QDs, and the changes in fluorescence intensity were observed. As shown in Fig. 5, a linear relationship of fluorescence intensity and *S. typhimurium* concentration in the range of 50–1000 CFU mL⁻¹ (Fig. 5A) and 100–1000 CFU mL⁻¹ (Fig. 5B) was achieved in PBS buffer and the cabbage sample, respectively, and the calculated LOD value in cabbage sample was 32 CFU mL⁻¹.

The specificity of biosensor is a common problem in immunological-based assay and in molecular-based identification, which might lead to a false positive result. Thus, the use of a highly specific aptamer biorecognition element could prevent such problems. In general, aptamer as a biorecognition element showed a good selectivity detection towards target analytes. The specificity of this study was examined in the presence of *Staphylococcus aureus*, *Escherichia coli*, *shawnelle oneidensis*, *enterobacter aerogenes*, *proteus mirabilis*, *citrobacter freundii*, *citrobacter diversus*, *enterobacter cloacae* and *bacillus*. As shown in Figure S6, a significant enhancement in fluorescence was observed for *S. typhimurium* whereas no such enhancement was found for *Escherichia coli*, *shawnelle oneidensis*, *enterobacter aerogenes*, *proteus mirabilis*, *citrobacter freundii*, *citrobacter diversus*, *enterobacter cloacae* and *bacillus* indicating the proposed sensing strategy to be highly selective towards *S. typhimurium*.

To assess the analytical performance of the present study, *S. typhimurium* was added to a fresh vegetable washing solution and used as samples for testing. We also studied the intra- and inter-day experiment to check the accuracy of the proposed method. Precision and accuracy were assessed by replicate analysis (n = 6) of spiked samples at different concentrations. A unifactorial ANOVA was carried out to evaluate if there were statistically significant differences between the fluorescence intensity values of the spherical and non-spherical surfaces, two tests in a day, tests in different days. The results showed that the fluorescence assay rough morphology presented higher fluorescence intensity values than those of smooth surfaces, with statistically significant differences (p-value of 0.018). Moreover, a one-way ANOVA was performed to assess whether there were statistically significant differences between the intraday assay and intraday fluorescence assay values

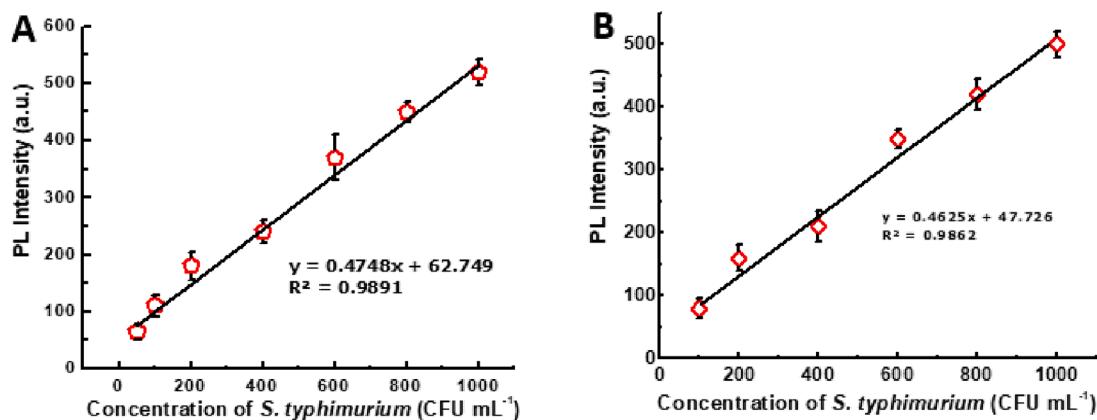


Fig. 5. Detection of *S. typhimurium* in PBS (A) and crushed cabbage sample (B).

from the rough surfaces. No differences were observed in this case since there were p-value of 0.37 and 0.41, respectively. Hence, the proposed method is highly reproducible, repeatable, and well-fitted to apply in real-life application in complex media.

As presented in Table 1, the intraday and interday precisions were between 2 % and 5 % and the detection of *S. typhimurium* in the spiked sample has a satisfactory percent recovery of 98.00 % to 104.22 %, with an RSD value of less than 4.0 %. These results revealed that the proposed detection method is highly precise and trustworthy for the detection of *S. typhimurium* in real life samples.

The proposed detection method was validated with a commercial kit (CD Creative Diagnostics, USA). The assay protocol and sample preparation were strictly followed as mentioned in the product manual. As shown in Table S2, the detection performance of the proposed method was superior to the commercial one. Moreover, a comparison study with the reported article for *S. typhimurium* detection has been presented in Table S3 that revealed the present study is comparable to other reported articles. Most importantly, the synthesized nanoparticles were stable upto one year. As shown in Table S4, zeta potential values were unchanged upto one year revealing the stability of nanoparticles. The proposed assay showed 95 % reproducibility with different batches of nanoparticles (Table S5).

4. Conclusion

In this study, we have reported spherical and urchin-like $\text{Fe}_3\text{O}_4@\text{Au}$ core-shell NPs that exhibited strong magnetization and plasmonic properties. Moreover, we elucidated the changes in fluorophore emission on spherical and urchin-like $\text{Fe}_3\text{O}_4@\text{Au}$ core-shell NPs using an LBL electrostatic self-assembly technique to create distance between the metal and the Au QDs. We found more than twofold enhancement in PL emission and a shorter lifetime of QDs on urchin-like gold film (3.23 ± 0.06 ns) compared to the spherical gold film (4.10 ± 0.10 ns). Furthermore, the fluorescence enhancement effect was utilized for *S. typhimurium* detection in a cabbage sample derived from commercially available sources. An LOD value of 32 CFU mL^{-1} was achieved for *S. typhimurium* detection in a spiked cabbage sample. A satisfactory percent recovery of 98.00 % to 104.22 %, with an RSD value of less than 4.0 % in spiked samples indicated the practicability of the present study. It is common that fluorescence method is much faster than electrochemical and colorimetric method. The proposed assay would be much easier and economical while integrated with portable instrument. We believe that the proposed fluorescence immunoassay format can be applied for the detection of other targets and would be promising technology in replacing the conventional immunoassay. However, one potential limitation of the fluorescence-based assay is the quenching of emission. The application of core-shell QDs might be a possible way to overcome this drawback. More research data on the stability of

Table 1

Relative standard deviation (RSD%), accuracy and recovery study of the *S. typhimurium* in spiked sample.

Sample	Labelled (CFU mL ⁻¹)	Found (CFU mL ⁻¹)	Accuracy (Bias)	Recovery (%)	RSD (%)
1	100	102.20	2.1	102.20	3.15
2	80	83.38	3.5	104.22	2.97
3	60	62.50	2.8	104.16	3.48
4	40	39.20	4.1	98.00	3.28

nanomaterials in different environment and (pH, temperature), reproducibility of synthesis method among different batch is needed before its application in real-life. Moreover, the miniaturized instrument integrated with dark chamber (detection zone, to protect light) and photomultiplier tube (to multiply the generated light in detectable form) is highly desirable.

CRedit authorship contribution statement

Abdulhakeem Alzahrani: Conceptualization, Investigation, Methodology, Resources, Supervision, Validation, Visualization, Writing – original draft. **Tawfiq Alsulami:** Conceptualization, Investigation, Software, Visualization, Writing – original draft, Writing – review & editing. **Ahmad Salamatullah:** Formal analysis, Methodology, Resources, Visualization, Writing – review & editing. **Hind Saeed Alzahrani:** Conceptualization, Visualization, Writing – review & editing.

Declaration of competing interest

The authors declare that they have no known competing financial interests or personal relationships that could have appeared to influence the work reported in this paper.

Acknowledgments

The authors would like to extend their sincere appreciation to the Researchers Supporting Project, King Saud University, Riyadh, Saudi Arabia, for funding this work through the project number (RSPD2024R589).

Appendix A. Supplementary data

Supplementary data to this article can be found online at <https://doi.org/10.1016/j.jksus.2024.103211>.

References

- Adhikari, M., Echeverria, E., Risica, G., McIlroy, D.N., Nippe, M., Vasquez, Y., 2022. Synthesis of magnetite nanorods from the reduction of iron oxyhydroxide with hydrazine. *ACS Omega* 5, 22440–22448. <https://doi.org/10.1021/acsomega.0c02928>.
- Ahghari, M.R., Amiri-khamakani, Z., Ali Maleki, A., 2023. Synthesis and characterization of Se doped Fe₃O₄ nanoparticles for catalytic and biological, properties. *Sci. Rep.* 13, 1007. <https://doi.org/10.1038/s41598-023-28284-x>.
- Ahmed, S.R., Chand, R., Kumar, S., Mittal, N., Srinivasan, S., Rajabzadeh, A.R., 2020. Recent biosensing advances in the rapid detection of illicit drugs. *TrAC Trends Anal. Chem.* 131, 116006.
- Ahmed, S.R., Cardoso, A.G., Kumar, S., Ortega, G.A., Srinivasan, S., Rajabzadeh, A.R., 2021. Nanozymes in biosensing and bioimaging. *CRC Press, Chapter 7*, 115–143.
- Ahmed, A.R., Hossain, M.A., Park, J.Y., Kim, S., Lee, D., Suzuki, T., Lee, L., Park, E.Y., 2014. Metal enhanced fluorescence on nanoporous gold leaf-based assay platform for virus detection. *Biosens. Bioelectron.* 58, 33–39. <https://doi.org/10.1016/j.bios.2014.02.039>.
- Ahmed, A.S., Mogus, J., Chand, R., Nagy, É., Neethirajan, S., 2018. Optoelectronic fowl adenovirus detection based on local electric field enhancement on graphene quantum dots and gold nanobundle hybrid. *Biosens. Bioelectron.* 103, 45–53. <https://doi.org/10.1016/j.bios.2017.12.028>.
- Ahmed, S.R., Nagy, É., Neethirajan, S., 2017. Self-assembled star-shaped chiroplasmonic gold nanoparticles for the ultrasensitive chiro-immunosensor for viruses. *RSC Adv.* 7, 40849–40857. <https://doi.org/10.1039/C7RA07175B>.
- Ahmed, S.R., Sherazee, M., Srinivasan, S., Rajabzadeh, A.R., 2022. Nanozymatic detection of thiocyanate through accelerating the growth of ultra-small gold nanoparticles/graphene quantum dots hybrids. *Food Chemistry* 379, 132152.
- Ahmed, S.R., Sherazee, M., Das, P., Shalauddin, M., Akhter, S., Basirun, W.J., Srinivasan, S., Rajabzadeh, A., 2024. Electrochemical assisted enhanced nanozymatic activity of functionalized borophene for H₂O₂ and tetracycline detection. *Biosens. Bioelectron.* 246, 115857.
- Ahmed, A.R., Takemura, K., Li, T., Kitamoto, N., Tanaka, T., Suzuki, T., Park, E.Y., 2017. Size-controlled preparation of peroxidase-like graphene-gold nanoparticle hybrids for the visible detection of norovirus-like particles. *Biosens. Bioelectron.* 87, 558–565. <https://doi.org/10.1016/j.bios.2016.08.101>.
- Alzahrani, A., Alsulami, T., Salamattullah, A.M., Ahmed, A.R., 2023. A non-spherical gold nanoparticles enhanced fluorescence of carbon dots for norovirus-like particles detection. *J. Biol. Eng.* 17, 1–9. <https://doi.org/10.1186/s13036-023-00351-x>.
- Baniukevic, J., Boyaci, I.H., Bozkurt, A.G., Tamer, U., Ramanavicius, A., Ramanaviciene, A., 2013. Magnetic gold nanoparticles in SERS-based sandwich immunoassay for antigen detection by well oriented antibodies. *Biosens. Bioelectron.* 43, 281–288. <https://doi.org/10.1016/j.bios.2012.12.014>.
- Cheng, S., Shao, J., Huang, B., Guan, J., Zhou, L., 2020. Promotion effect of urchin-like MnOx@PrOx hollow core-shell structure catalysts for the low-temperature selective catalytic reduction of NO with NH₃. *RSC Adv.* 10, 13855–13865. <https://doi.org/10.1039/D0RA00668H>.
- Ehuwa, O., Jaiswal, A.K., Jaiswal, S., Salmonella, S., 2021. Food safety and food handling practices. *Foods* 10, 907. <https://doi.org/10.3390/foods10050907>.
- Y. Eremin, A. Doicu, T. Wriedt. Extension of the discrete sources method to investigate the non-local effect influence on non-spherical core-shell particles, 235(2019), 300–308. DOI: 10.1016/j.jqsrt.2019.07.012.
- Félix, L.L., Sanz, B., Sebastián, V., Torres, T.E., Sousa, M.H., Coaquira, J.A.H., Ibarra, M. R., Goya, G.F., 2019. Gold-decorated magnetic nanoparticles design for hyperthermia applications and as a potential platform for their surface functionalization. *Sci. Rep.* 9, 4185. <https://doi.org/10.1038/s41598-019-40769-2>.
- Gessner, I., Park, J., Lin, H., Lee, H., Weissleder, R., 2022. Magnetic gold nanoparticles with idealized coating for enhanced point-of-care sensing. *Adv. Healthc. Mater.* 11, e2102035.
- Habib, I., Khan, M., Mohamed, M.I., Ghazawi, A., Abdalla, A., Lakshmi, G., Elbediwi, M., Marzooqi, H.M.A., Afifi, H.S., Shehata, M.G., Al-Rifai, R., 2023. Assessing the prevalence and potential risks of Salmonella infection associated with fresh salad vegetable consumption in the United Arab Emirates. *Foods* 12, 3060. <https://doi.org/10.3390/foods12163060>.
- Han, Z., Pan, Y., Chen, S., Wei, X., 2023. Time-resolved FRET-based immunosensor for the ultrasensitive and rapid detection of Cd²⁺. *J. Agric. Food Chem.* 71 (29), 11195–11203. <https://doi.org/10.1021/acs.jafc.3c01535>.
- Li, D., Zuo, X., Zhang, X., Tang, Y., Zhao, X., Zhang, Y., Yang, H., 2023. Emerging urchin-like core-shell mineral microspheres with efficient photothermal conversion and solar energy storage. *J. Energy Storage* 68, 107661. <https://doi.org/10.1016/j.est.2023.107661>.
- Myndrul, V., Viter, R., Savchuk, M., Koval, M., Starodub, N., Silamiķelis, V., Smyntyna, V., Ramanavicius, A., Iatsunskyi, I., 2017. Gold coated porous silicon nanocomposite as a substrate for photoluminescence-based immunosensor suitable for the determination of Aflatoxin B1. *Talanta* 175, 297–304. <https://doi.org/10.1016/j.talanta.2017.07.054>.
- Viter, R., Savchuk, M., Iatsunskyi, I., Pietralik, Z., Starodub, N., Shpyrka, N., Ramanaviciene, A., Ramanavicius, A., 2018. Analytical, thermodynamical and kinetic characteristics of photoluminescence immunosensor for the determination of Ochratoxin A. *Biosens. Bioelectron.* 99, 237–243. <https://doi.org/10.1016/j.bios.2017.07.056>.
- Wang, Q., Cheng, X., Li, H., Yu, F., Wang, Q., Yu, M., Liu, D., Xia, J.J., 2020. A novel DNA quantum dots/aptamer-modified gold nanoparticles probe for detection of Salmonella typhimurium by fluorescent immunoassay. *Mater. Today Commun.* 25, 101428. <https://doi.org/10.1016/j.mtcomm.2020.101428>.
- Wu, M., Rao, L., Liu, L., Li, Y., Zhang, Y., Ji, Z., Ying, G., 2023. Urchin-like Fe₃O₄@C hollow spheres with core-shell structure: Controllable synthesis and microwave absorption. *J. Colloid Interface Sci.* 649, 313–324. <https://doi.org/10.1016/j.jcis.2023.06.077>.